



# Nanostructured Dielectric Fractals on Resonant Plasmonic Metasurfaces for Selective and Sensitive Optical Sensing of Volatile Compounds

Zelio Fusco, Mohsen Rahmani,\* Renheng Bo, Ruggero Verre, Nunzio Motta, Mikael Käll, Dragomir Neshev, and Antonio Tricoli\*

Advances in the understanding and fabrication of plasmonic nanostructures have led to a plethora of unprecedented optoelectronic and optochemical applications. Plasmon resonance has found widespread use in efficient optical transducers of refractive index changes in liquids. However, it has proven challenging to translate these achievements to the selective detection of gases, which typically adsorb non-specifically and induce refractive index changes below the detection limit. Here, it's shown that integration of tailored fractals of dielectric TiO<sub>2</sub> nanoparticles on a plasmonic metasurface strongly enhances the interaction between the plasmonic field and volatile organic molecules and provides a means for their selective detection. Notably, this superior optical response is due to the enhancement of the interaction between the dielectric fractals and the plasmonic metasurface for thickness of up to 1.8 μm, much higher than the evanescent plasmonic near-field (≈30 nm). Optimal dielectric–plasmonic structures allow measurements of changes in the refractive index of the gas mixture down to  $<8 \times 10^{-6}$  at room temperature and selective identification of three exemplary volatile organic compounds. These findings provide a basis for the development of a novel family of dielectric–plasmonic materials with application extending from light harvesting and photocatalysts to contactless sensors for noninvasive medical diagnostics.

such as gold, silver, copper, and aluminum, are used as transducer for changes in the refractive index of their surroundings.<sup>[1]</sup> The high local sensitivity of this sensing mechanism arises from the strong evanescent field, which decays within the first 6–30 nm<sup>[2,3]</sup> from the nanoparticles surface. As a result, LSPR sensors can easily detect very low concentrations of chemicals and biomolecules,<sup>[4]</sup> which are mainly concentrated near the metal surface where the plasmonic fields are strongest. Application of LSPR to the rapidly growing area of gas molecule sensing has proven difficult due to their lack of sensibility toward small refractive index changes, induced by most volatile compounds, and the challenge to discern between the optical responses to different analytes. For instance, application of LSPR to noninvasive medical diagnostics via breath analysis would require detection of specific volatile organic compounds down to particle per million concentrations, corresponding to variations of less  $<10^{-5}$  in refractive index, in complex gas mixtures.<sup>[5]</sup>

Localized surface plasmon resonance (LSPR) is being increasingly used as a powerful mechanism for the optical sensing of important chemical and biological compounds in liquid environments. In LSPR devices, the change in the resonant collective oscillations of free electrons of metal nanostructures,

A variety of metal nanostructures and morphologies have been proposed to improve the LSPR sensing performances.<sup>[6,7]</sup> Liu et al. have shown that the gas-phase sensitivity toward H<sub>2</sub> can be improved via the utilization of nanoscale layout comprising a palladium nanodisk absorption layer and a gold

Z. Fusco, R. Bo, Prof. A. Tricoli  
Nanotechnology Research Laboratory  
College of Engineering and Computer Science  
The Australian National University  
ACT 2601, Australia  
E-mail: antonio.tricoli@anu.edu.au  
Dr. M. Rahmani, Prof. D. Neshev  
Nonlinear Physics Centre  
Research School of Physics and Engineering  
The Australian National University  
ACT 2601, Australia  
E-mail: mohsen.rahmani@anu.edu.au

Dr. R. Verre, Prof. M. Käll  
Department of Physics  
Chalmers University of Technology  
412 96 Göteborg, Sweden  
Prof. N. Motta  
Institute for Future Environments and School of Chemistry, Physics, and  
Mechanical Engineering  
Queensland University of Technology  
Brisbane, QLD 4001, Australia

DOI: 10.1002/adma.201800931

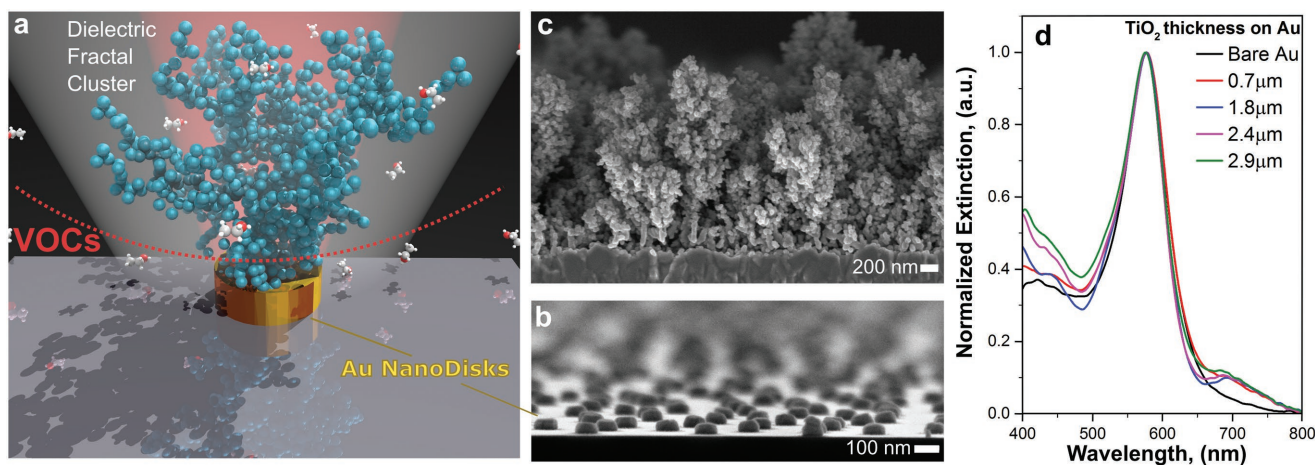


**Figure 1.** Dielectric fractals-plasmonic LSPR sensors. a) Simplified schematic of the fractal TiO<sub>2</sub>-Au nanodisks layout emphasizing the morphology of a single TiO<sub>2</sub> fractal (not in scale). The real devices consist of multiple TiO<sub>2</sub> fractals deposited both on the Au nanodisks and on the surrounding glass surface (Figure S7, Supporting Information). b) Cross-section SEM image in tilted view of an Au nanodisk metasurface with an in-plane diameter of 100 nm and a thickness of 40 nm. c) Cross-section SEM image of the engineered TiO<sub>2</sub> dielectric fractals with a porosity of 98% and a thickness of 1.8 μm. d) Optical characterization of the dielectric fractals-plasmonic sensors as a function of the TiO<sub>2</sub> thicknesses. Integration of these highly porous TiO<sub>2</sub> fractals on the Au metasurface does not affect the LSPR peak position up to a thickness of more than 2.9 μm.

nanoantenna.<sup>[8]</sup> Bingham et al.<sup>[9]</sup> have demonstrated a high-resolution LSPR spectroscopy system with silver nanoparticles able to detect bulk refractive index changes as small as  $3 \times 10^{-4}$  measuring a plasmonic shift of 0.048 nm for switching from pure He to Ar. Integration of catalytic reactive layers on LSPR systems has been pursued by numerous approaches such as sputtering, electron-beam deposition and sol-gel.<sup>[10,11]</sup> Contrary to the direct LSPR sensing, in these systems the metal nanoparticles act as a reactive surface for interaction with the gas molecules, resulting in a variation in the optical properties of the catalytic material via charge-transfer processes at relatively high temperatures.<sup>[10,12]</sup> Alternatively, integration of 2D materials has been achieved mainly for surface enhanced Raman spectroscopy demonstrating the enhancement of the electric field without suppressing its propagation.<sup>[13]</sup>

As an alternative approach, the integration of dielectric materials on resonant metal nanostructures is being investigated as a means to optimally couple plasmonic and photonic materials.<sup>[14]</sup> Although several different methods have been developed to integrate metallic nanoparticles into periodic dielectric structures,<sup>[15]</sup> or embedding them in porous dielectric materials,<sup>[16]</sup> amplification of the optical sensing properties of these devices is still insufficient, due to the low dielectric contrast and degree of order.<sup>[16]</sup> Furthermore, a facile and controllable strategy for the large-scale production of well performing dielectric-metal LSPR sensors is lacking. In this context, integration of intrinsically scale-invariant fractals made of wide bandgap semiconductors<sup>[17,18]</sup> could provide a well-controlled and scalable approach to investigate the potential of LSPR-dielectric device for sensing of gas molecules.

Here, we use dielectric fractals of TiO<sub>2</sub> nanoclusters, with a fractal dimension of 1.8, to enhance the optical response of efficient plasmonic substrates (Figure 1a). This combination is sensitive to small variations in the refractive index of gas mixtures, allowing the detection of low concentrations of volatile organic compounds and providing an approach for their

identification. Self-assembly of 98% porous TiO<sub>2</sub> nanostructured fractals with controlled thickness from 0.7 to 2.9 μm on Au nanodisks surfaces was obtained by scalable and well-reproducible nanoparticle aerosol deposition (Figure 1b,c and Sections S1–S4, Supporting Information). The low effective refractive index of these nanostructured TiO<sub>2</sub> fractals minimizes the attenuation of the optical signal (Figure 1d and Section S6, Supporting Information), while providing a large surface area for the anchoring of the gas molecules and their interaction with the plasmonic field. We observe that an optimal fractal thickness of 1.8 μm leads to a fivefold increase in the shift of the plasmonic resonance, and increases the detection limit from 4% of the bare metasurfaces to 0.1 vol% of three test volatile organic compounds (VOCs). Simulations of the interaction of the plasmonic field with the dielectric fractals indicate an enhancement of the electric field in the proximity of the TiO<sub>2</sub> nanoparticles, as well as an increase of the sensing volume beyond the plasmonic sensing thickness of 30 nm. We use the temperature dependence of the VOCs adsorption equilibrium on the TiO<sub>2</sub> fractals to identify and distinguish between three common VOCs, namely, acetone, toluene, and ethanol, providing an approach for future engineering of selective gas-phase LSPR sensors.

Large-scale resonant Au substrates with monomers having an in-plane diameter ranging from 60 to 150 nm were obtained through hole-mask colloidal lithography (HCL) (see the Experimental Section and Sections S1 and S2 in the Supporting Information). Since the dimensions of the gold particles and the nearest neighbor distances are both sub-wavelength, the particles surface behaves optically as a homogeneous film (i.e., no higher diffractive orders and very weak diffuse scattering), which is commonly, and here, referred to as a metasurface. The fractals were directly self-assembled on the Au metasurfaces via direct deposition of flame-made TiO<sub>2</sub> nanoparticle aerosols in the diffusion regime. The fractal nature of these layers arises from the stochastic nature of the

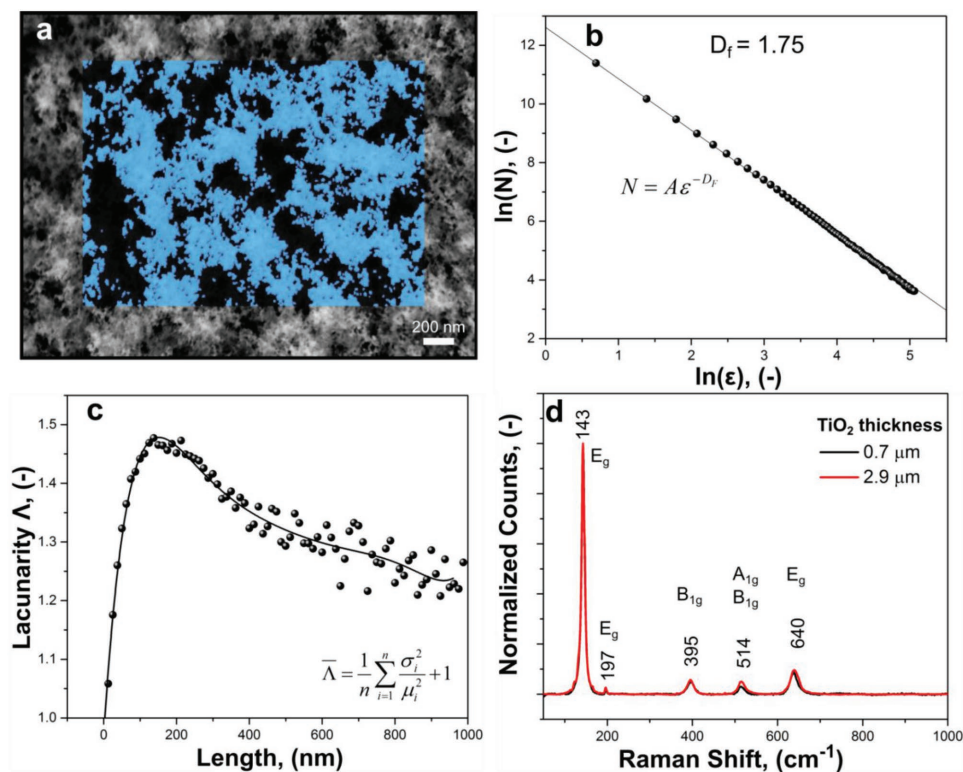


**Figure 2.** Characterization of the dielectric TiO<sub>2</sub> fractals. a) Top-view SEM image of a dielectric film made of TiO<sub>2</sub> fractals with an average thickness of 1.8 μm. The inset shows the fractal generated from the pixel analysis. b) Double-log plot of the foreground pixel number as a function of the scaling factor. The slope of the curve provides the fractal dimension ( $D_f = 1.75$ ). c) Lacunarity as evaluated by the pixel distribution of the image. The lacunarity is a parameter which quantifies the fractal morphological inhomogeneity and shows a maximum inhomogeneity in the range of 150–200 nm. Note that the pixel size is 6.25 nm. Hence, length (nm) =  $\epsilon$  (pixel)  $\times$  6.25 (nm pixel<sup>-1</sup>). d) Normalized Raman spectra of the thinnest and thickest fractals on the Au metasurfaces indicating the formation of an anatase TiO<sub>2</sub> phase.

nanoparticle aerosol deposition process, where since the early stage the structures begin to ramify.<sup>[19–21]</sup> This leads to a highly porous and uniform fractals with tuneable thickness and identical primary particle size and composition.<sup>[17]</sup> A peculiar characteristic of the presented fractals is their stochastic self-similarity for all thickness implemented here. In fact, upon a distance of three particle diameter from the surface, equivalent to  $\approx 20$ – $30$  nm here, the nanoparticle aerosol deposition leads to three-dimensionally disorganized structures composed of surface-bond agglomerates having scale-invariant features.<sup>[20]</sup> Notably, in the diffusion regime, the self-assembly of the nanoparticle aerosols on the surface leads to an average film porosity of  $\approx 98\%$ .<sup>[22]</sup> The high porosity and surface area of these fractals provide a unique opportunity for the efficient trapping of gas molecules and possibly to increase the effective change in refractive index for LSPR sensing.

**Figure 2a** shows the generated fractal obtained from the pixel distribution of a representative scanning electron microscope (SEM) image of a 1.8 μm thick TiO<sub>2</sub> film on a plasmonic metasurface. Two key parameters to define the fractal space are the fractal dimension and lacunarity. The fractal dimension,  $D_f$ , is a dimensionless number, which measures the degree of complexity of a system providing the likelihood that an object is invariant at different scales. It can be evaluated by applying the following fractal power law<sup>[23]</sup>

$$N = k_0 \left( \frac{R_g}{r} \right)^{D_f} \quad (1)$$

where  $N$  is the number of monomers with radius  $r$ , which is proportional to the mass of the system,  $R_g$  is the gyration radius, i.e., a spatial distribution of mass in the aggregate, and  $k_0$  is a constant prefactor of the order of unity. By estimating  $R_g/r$  with the number of pixel ( $\epsilon$ ), Figure 2b visualizes the  $D_f$  of the TiO<sub>2</sub> fractals as the slope of the  $\ln(N)$  versus  $\ln(\epsilon)$  plot, which results in a  $D_f$  of 1.75. This is in agreement with recent reports on the  $D_f$  of fractals generated by Brownian's collision of nanoparticle aerosols,<sup>[24,25]</sup> confirming the diffusion-limited cluster–cluster aggregation as the driving mechanism for the film self-assembly.<sup>[25,26]</sup>

The lacunarity,  $\Lambda$ , quantifies the fractal morphological inhomogeneity. It represents the heterogeneity and the textures of a fractal indicating how the fractal space is filled with gaps: the higher the lacunarity the lower the homogeneity. Here, the mean  $\Lambda$  has been evaluated from the mean,  $\mu$ , and the variance,  $\sigma^2$ , of the foreground pixels in the image (Figure 2a, and Section S7, Supporting Information). Notably, the plot of the lacunarity versus the analyzed box length (Figure 2c) shows a peak indicating a maximum level of inhomogeneity in the range of 150–200 nm. This provides an estimate of the maximum anisotropy achieved during cluster–cluster

coagulation in the aerosol, and indicates a value for the radius of gyration. From the fractal interpretation of the dielectric  $\text{TiO}_2$  is possible to indirectly estimate the specific surface area (SSA) and the porosity (see Section S7 and Figure S7, Supporting Information). Notably, these values are in good agreement with the experimental results obtained from the Brunauer–Emmett–Teller (BET) measurements of  $\text{TiO}_2$  nanoparticles collected from the flame-made aerosols with backhouse filters. The isotherms of nitrogen adsorption and desorption of these particles reveal a BET surface area of  $126 \text{ m}^2 \text{ g}^{-1}$  (Figure S7, Supporting Information), in good agreement with previous studies of flame-made anatase  $\text{TiO}_2$  nanoparticles made in similar conditions. The corresponding BET particle diameter assuming a spherical particle shape (see Section S7, Supporting Information) is  $11.2 \text{ nm}$ , and thus in good agreement with the particle size distribution and mean particle size of  $10.58 \text{ nm}$  computed from the transmission electron microscopy (TEM) measurements (Figure S5, Supporting Information). The average  $\text{TiO}_2$  film porosity was computed by gravimetric and cross-sectional SEM analysis revealing an average  $\text{TiO}_2$  film porosity of  $\approx 98\%$ , in excellent agreement with previous theoretical<sup>[19]</sup> and experimental studies.<sup>[27]</sup> These high SSA and porosity are a key factor for promoting a deep and reversible diffusion of the gas

molecules in the dielectric fractal film, enhancing the effective change in refractive index interacting with the plasmonic metasurfaces.

Raman spectroscopy was performed to confirm the fractal composition as a function of the film thickness confirming a pure anatase  $\text{TiO}_2$  composition. The TEM characterization reveals a mostly spherical particle shape and a highly crystalline composition of the primary particles (Figure S4a–c, Supporting Information), in line with previous studies on flame-made  $\text{TiO}_2$ .<sup>[17]</sup> The particle size distribution (Figure S4d, Supporting Information) was evaluated from the TEM images counting 218 primary particles, and revealed a typical Gaussian-shaped unimodal distribution with a mean particle diameter,  $d_p$ , of  $10.58 \text{ nm}$  and a geometric standard deviation of  $1.32$ . Figure 2d (and Figure S5, Supporting Information) shows the characteristic active Raman modes of anatase  $\text{TiO}_2$  for both the thinnest and thickest film. This is in line with previous reports on the flame synthesis and aerosol deposition of  $\text{TiO}_2$  films,<sup>[28]</sup> indicating a successful fabrication of  $\text{TiO}_2$  fractal films with identical composition from an average thickness of  $0.7$  to  $2.9 \mu\text{m}$ .

Figure 3 summarizes the use of the dielectric fractal-LSPR sensors for the measurement of ethanol, a standard test volatile

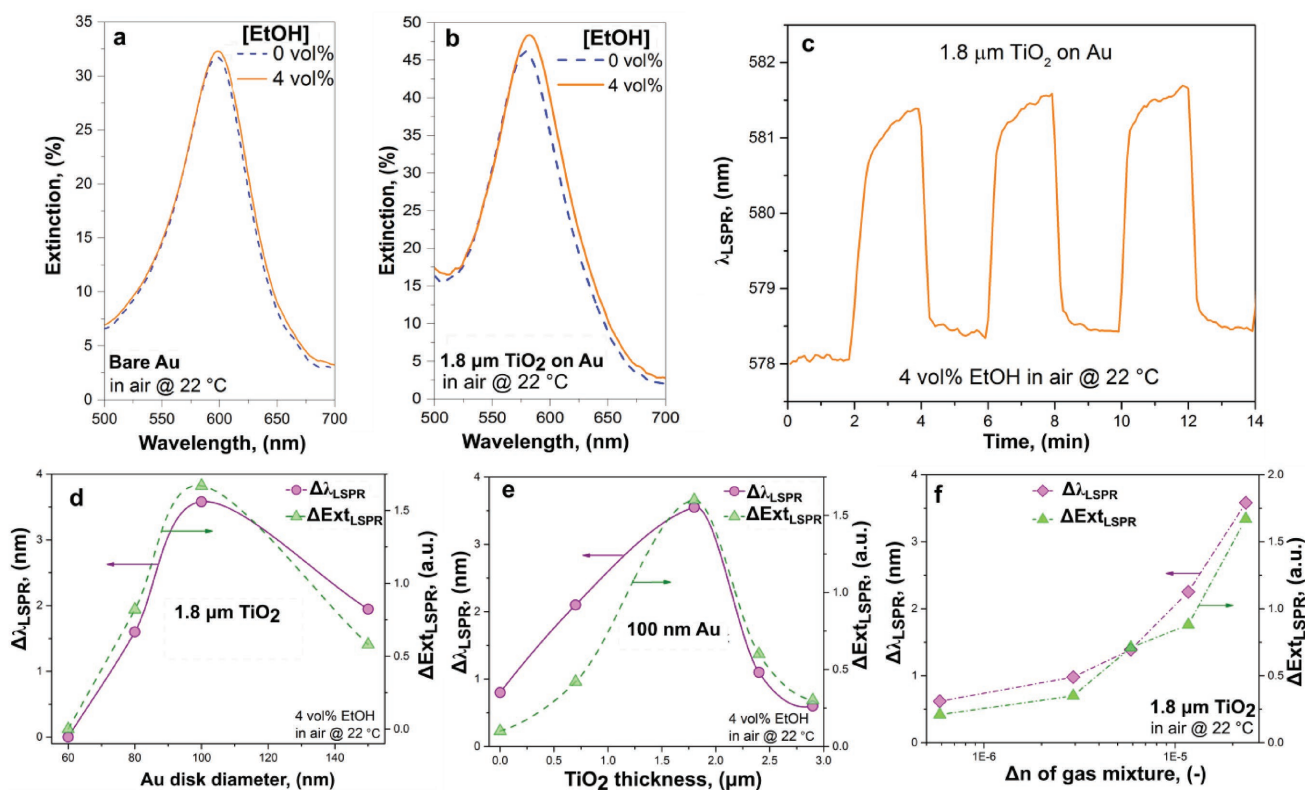


**Figure 3.** Dielectric fractal-enhanced LSPR sensing of gas molecules. a) The extinction spectra in air for the bare  $100 \text{ nm}$  diameter Au shows a small shift upon  $4 \text{ vol}\%$  EtOH injection at room temperature. b) The plasmonic shift is enhanced when a  $1.8 \mu\text{m}$  thick  $\text{TiO}_2$  fractal film is deposited on the same Au metasurfaces. c) Dynamic response of the resonance peak position of a  $1.8 \mu\text{m}$  thick  $\text{TiO}_2$  fractal film on the  $100 \text{ nm}$  Au disk array to different cycles of air/EtOH with a concentration of  $4 \text{ vol}\%$  at room temperature. d) Plasmonic shift and extinction difference of  $1.8 \mu\text{m}$  thick  $\text{TiO}_2$  layer as a function of the Au disk diameter with  $4 \text{ vol}\%$  EtOH in air at room temperature. e) The optimized  $100 \text{ nm}$  disk array has been chosen to analyze the effect of  $\text{TiO}_2$  layer: plasmonic shift and extinction difference were recorded as a function of the layer thickness, showing optimum coupling for  $1.8 \mu\text{m}$  thick layer. f) Limit of detection for the optimized sample as a function of the change in the gas-phase refractive index shows very high sensitivity to the local environment. Note the logarithmic scale on the x-axis.

organic compound, in air at room temperature. Figure 3a,b shows the characteristic extinction spectra of a bare and a TiO<sub>2</sub> fractal-enhanced Au metasurface in air and upon injection of 4 vol% of EtOH gas. The change in the dielectric environment from air ( $n = 1.000292$ ) to 4 vol% ethanol ( $n = 1.000878$ ), corresponds to a refractive index change of the gas mixture of ( $\Delta n$ )  $2.3 \times 10^{-5}$ . Notably, while the increase in refractive index always induces a redshift of the plasmonic resonance, the fractal-enhanced Au metasurface shows a five times higher increase in the plasmonic shift than the bare one, resulting in a variation of 3.6 nm in the peak position. Figure 3c shows the peak position of a representative fractal-enhanced Au metasurface during several cycles of ethanol on/off switching in air. These devices promptly responds to multiple injections of 4 vol% of EtOH in air at room temperature showing good reproducibility with a cycle-to-cycle and batch-to-batch variation of the LSPR shift of below 5% (see Section S8, Supporting Information). Upon gas purging, the device readily reacts to the local refractive index change showing a fast response and recovery time, both of the order of 10 s. This fast response dynamics is attributed the 98% porosity, which enables a facile and reversible adsorption of the gas molecules in the whole fractal film.

Optimization of the interaction of the dielectric fractal structure with the plasmonic metasurfaces for LSPR sensing of VOCs was pursued as a function of the Au nanodisks diameters and TiO<sub>2</sub> fractal average thickness. First, the LSPR response of different Au nanodisk arrays with a diameter from 60 to 150 nm, coated with a fixed TiO<sub>2</sub> fractal thickness of 1.8  $\mu\text{m}$ , to cycles of synthetic air and 4 vol% EtOH at room temperature was investigated. Figure 3d summarizes the results in terms of plasmonic shift and extinction difference. Relevant simulation results can be found in Figure S9 (Supporting Information). It was found that the strongest coupling between the Au metasurface and the dielectric fractals is obtained with the 100 nm Au array, resulting in the maximum LSPR peak shift. Figure 3e shows the plasmonic shift and extinction difference as a function of the thickness of the TiO<sub>2</sub> fractals from 0 to  $\approx 3 \mu\text{m}$  on the optimal 100 nm Au disks metasurfaces. Notably, while both the plasmonic shift and extinction were increased for any TiO<sub>2</sub> thicknesses, an optimal fractal thickness of 1.8  $\mu\text{m}$  was observed. Despite this fractal thickness is significantly larger than the 30 nm LSPR electromagnetic field decay length,<sup>[9]</sup> it still resulted in an increase of the overall LSPR sensitivity.

The lower limit of detection of these fractal-enhanced Au metasurfaces LSPR sensors was investigated decreasing the ethanol concentration from 4 to 0.1 vol%. Figure 3f summarizes the changes in plasmonic shift and extinction difference as a function of the change in refractive index of the gas mixture. Notably, the fractal-LSPR coupling allowed to discern changes in the refractive index of the gas mixture down to less than  $10^{-5}$  at room temperature. A linear fit of the  $\Delta\lambda$  versus  $\Delta n$  plot provides a sensitivity (slope of the curve) of 137345 nm RIU<sup>-1</sup> (see Section S8, Supporting Information). In comparison, the bare Au metasurfaces had a reliable lower limit of detection of 4 vol% (see Section S10, Supporting Information). With respect to recent high performing LSPR sensors for detection of gas molecules, the sensitivity,

reported here, for the fractal-enhanced dielectric structures is about 4–8 times higher.<sup>[9,29]</sup>

The enhancement is due to a twofold reason: first, the fractal system presents a large surface-to-volume ratio which increases the condensation probability of the volatile gases for the hybrid systems. At the same time it observed an extension of the effective sensing volume to several hundreds of nanometers. The first one is suggested by the Figure 3e: clearly, the sensitivity increases up to a certain thickness. Afterward, it decreases due to difficulty for the volatile gas to penetrate inside the fractal dielectric and diffuse to the active sensing region.

To gain insight on the second mechanism for the fractal-enhanced LSPR devices, we performed a set of electrodynamic simulations using finite-difference time-domain (FDTD) technique at room temperature (see also Section S9, Supporting Information). The enhancement of the electrodynamic field ( $\mathbf{E}$ ) with respect to the incident plane wave ( $\mathbf{E}_0$ ) above the Au metasurface was analyzed for a range of dielectric fractals with representative structural properties (TiO<sub>2</sub> nanoparticles of 10 nm) and compared to the bare Au nanodisks.

Figure 4a shows a schematic of the bare Au disk layout with a diameter of 100 nm. For the latter, the electric field shows a dipolar enhancement, characteristic of plasmonic structures (Figure 4b,c). Figure 4d shows the extension of the field orthogonally to the Au disk circumferential plane. A typical exponential decay of the  $|\mathbf{E}/\mathbf{E}_0|^2$  field was observed with a confinement in the first 17 nm above the Au surface.

As a model comparative structure, we analyzed the field behavior with two fractals having the lowest possible fractal dimension of  $D_f = 1$ , which is equivalent to a TiO<sub>2</sub> nanoparticle chain with 10 nm of diameter, separated by a 3 nm gap orthogonally aligned on top of the 100 nm diameter Au disk (Figure 4e). The two TiO<sub>2</sub> fractals with a  $D_f = 1$  have been investigated as an idealistic (case-limiting) situation for the smallest possible fractal dimension. For this purpose, different spacings between the two chains of TiO<sub>2</sub> monomers have been investigated (Section S9, Supporting Information). It was found that a gap value of 3 nm shows a slightly higher enhancement. This is attributed to the subwavelength regime of the dielectric TiO<sub>2</sub> nanoparticles, where the separation is small in comparison to the excited plasmonic field. We observed that the field bends inside the straight fractal chains (Figure 4f), resulting in a maximum amplification and propagation of the field between the chains' gap and increasing the sensing volume. Figure 4g shows the  $|\mathbf{E}/\mathbf{E}_0|^2$  in the gap between the TiO<sub>2</sub> chains as a function of the orthogonal distance from the Au disk circumferential plane. Notably, within the gap the field does not decay with the first 17 nm as per the bare Au, but retains a 4 times increase in the  $|\mathbf{E}/\mathbf{E}_0|^2$  amplification up to the end of the fractals structure at 400 nm above the Au surface. The TiO<sub>2</sub> chains cause an increase of the electric field both within the first 30 nm and at longer distances. Immediately above the Au surface, the amplitude drastically increases, showing a series of local electric field maxima corresponding to the closest point between the TiO<sub>2</sub> nanoparticles. Above 100 nm, due to the repetitive TiO<sub>2</sub> geometry, the gap intensity shows a periodic wave-like pattern along the length of the chains, with an average of 4 times intensity increase with respect to the incident plane wave.

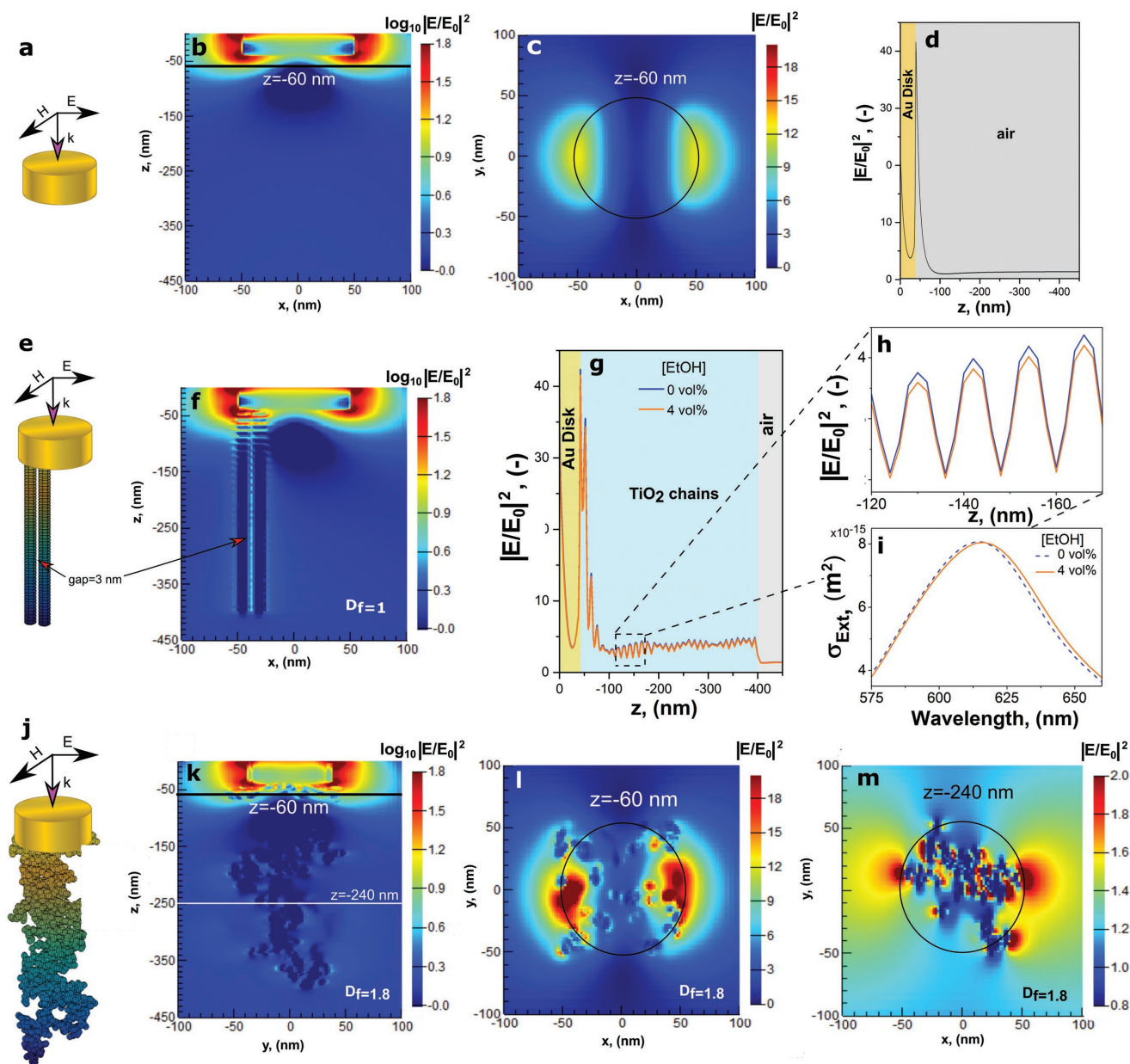


**Figure 4.** Electrodynamic simulations of the fractal-enhanced LSPR sensors. a) Schematic model of the simulated 100 nm Au nanodisk with the interacting plane wave. b) Cross-section and c) top view at 20 nm from the top Au edge of the enhancement of the dipolar electric field. d) Plasmonic field decay as a function of the distance from the disk for the bare disk. e) Schematic of the simulated simplified model consisting of two nanoparticles' chains ( $D_f = 1$ ) of  $\text{TiO}_2$  with a particle radius of 5 nm separated by 3 nm and deposited onto the Au disk with an in-plane diameter of 100 nm. f) Cross-section of the idealistic model showing an enhancement of the electric field in the gap between the chains. The electric field is bended and amplified in the proximity of the disk. g)  $|E/E_0|^2$  enhancement in the middle of the gap between two ideal  $\text{TiO}_2$  chain-like fractals with a  $D_f$  of 1 and a distance of 3 nm at the  $\lambda_{\text{LSPR}}$  as a function of the distance from the Au nanodisk in air (blue line) and with 4% of EtOH (orange line) at room temperature. The enhancement as a function of the distance between the fractal chains is reported in Figure S9a (Supporting Information). h) Magnification of (g) shows a regular pattern due to the  $\text{TiO}_2$  nanoparticles and the steep refractive index change. i) Simulated extinction cross-section for the idealistic model in air (blue line) and with 4 vol% of EtOH (orange dashed line) at room temperature. j) Not to scale, the schematic of the simulated model of the Au disk with an in-plane diameter of 100 nm and a  $\text{TiO}_2$  cluster from particle dynamic simulations with a realistic  $D_f$  of 1.8 and particle size of 10 nm. k–m) Cross-section (k) and top-view images (l,m) at 20 and 200 nm from the Au disk, respectively, of the  $|E/E_0|^2$  enhancement for the realistic fractal cluster model. The hybrid device shows high amplification of the field which is confined in the gap between of the nanoparticles.

Figure 4h shows the change in  $|E/E_0|^2$ , switching the environment from pure air to 4 vol% of EtOH, and it indicates a similar pattern but a slight decrease in the field intensity (Figure 4g,h).

This effect was also analyzed from a far-field perspective via evaluation of the extinction cross-section. Interestingly, in air the electric field intensity is always higher with respect to the

presence of the analyte: the increase in the refractive due to the gas causes a decrease in intensity. Notably, this decrease in the field energy is reflected in a shift of the LSPR peak to longer wavelength (Figure 4i), in agreement with the experimental measurements. The results obtained with these model TiO<sub>2</sub> chains, having a  $D_f = 1$ , show the contribution of the dielectric fractals in increasing the effective sensing volume.

Next, we extended our simulations to a more realistic TiO<sub>2</sub> fractal–Au disk system. The latter consisted of a fractal cluster with  $D_f = 1.8$  deposited on a 100 nm diameter Au nanodisk (Figure 4l). The dielectric cluster was obtained from particle dynamic simulation of nanoparticle aerosol self-assembly in the diffusion regime, as described in detail elsewhere,<sup>[20]</sup> and is a representative morphology for the TiO<sub>2</sub> fractals used here.<sup>[30]</sup> Figure 4m shows the electric field in a vertical cross-sectional plane to the Au disk circumference, while Figure 4n,o shows the parallel cross-sections at 20 and 200 nm above the Au disk. The latter provide a direct comparison with the bare Au (Figure 4c), indicating an enhancement of the electric field also inside this more realistic fractal cluster.

For the FDTD simulation with the two straight chains of fractals having a fractal dimension ( $D_f$ ) of 1, the strongest field enhancement is observed between the two chains once the distance between the chains' center axes is 3 nm. This optimal distance cannot be confirmed for the most realistic fractal dimension of 1.8, as in these disordered structures there is a broad range of interparticle spacing. The low fractal dimension of the TiO<sub>2</sub> nanostructures provides a very porous, high refractive index layer above the Au disks. This enables the redistribution of the dipolar plasmonic field, where the pull from the glass substrate is now partially balanced by the pull toward the high refractive index TiO<sub>2</sub> layer above the Au disks.<sup>[7]</sup> Thus, this porous TiO<sub>2</sub> layer morphology may promote an enhancement of the optical sensor response via confinement and enhancement between the TiO<sub>2</sub> high index fractal structures, which is also the location of the strongest interaction with the gas molecules (e.g., where the condensation may occur for the VOCs). Thus, this porous TiO<sub>2</sub> layer morphology may promote an enhancement of the optical sensor response via confinement and enhancement of the field between the TiO<sub>2</sub> high index fractal structures. More analysis of field enhancement can be seen in Figure S9 (Supporting Information). To further investigate the impact of the fractal morphology, we have simulated and compared three more TiO<sub>2</sub> morphologies (Figure S10, Supporting Information): i) a denser fractal structure with a fractal dimension of 2.1 (porosity of 84%), which represents the most dense morphology possible for (ballistic) deposition of nanoparticle aerosols; ii) a randomly packed arrangement of the same TiO<sub>2</sub> nanoparticles (with a porosity of 36%); and iii) a fully dense TiO<sub>2</sub> film (porosity of 0%). The comparison between the two different fractals (Figure S10, Supporting Information) shows a lower field enhancement ( $|E/E_0|$ ) for the more dense fractal ( $D_f = 2.1$ ) independently of the distance from the Au disk. We believe that this is due to the lower porosity of the latter fractal structure that reduces the penetration of the field in the TiO<sub>2</sub> layer. A similar but stronger decrease of the field enhancement is observed for the randomly packed spheres morphology with the porosity of 36%. Notably, in line with these results, for the completely dense TiO<sub>2</sub> layer on the gold disks, it is noted that

the plasmonic field does not penetrate through the dielectric layer and a very small enhancement is observed only at the edges of the film due to the dipolar behavior of the plasmonic field. These simulations indicate that, independently of the fractal nature, a high porosity is beneficial in allowing the penetration of the field in the TiO<sub>2</sub> layer and that a completely dense TiO<sub>2</sub> film blocks the plasmonic field. To validate these simulations, we have investigated the response to EtOH and a denser TiO<sub>2</sub> top layer (porosity of ≈50%) deposited on the same Au nanodisks. The TiO<sub>2</sub> top layer was fabricated by drop-casting of a 0.03 M solution of the same flame-made TiO<sub>2</sub> nanoparticles, which were collected from the aerosol through a back-house glass fiber filters placed at 30 cm from the burner, on the Au metasurfaces. The optical response of these samples to decreasing ethanol concentrations from 4 to 2 vol% in air was measured at room temperature (Figure S11, Supporting Information). A lower limit of detection for EtOH of 3 vol% with a maximum  $\lambda_{\text{LSPR}}$  shift for 4 vol% of ≈1 nm was observed. The latter performance is significantly worse than that of the highly porous fractal TiO<sub>2</sub> deposited by aerosol deposition (Figure 3). These simulations and experimental results further indicate that a highly porous morphology of TiO<sub>2</sub> nanoparticles is beneficial in enhancing the plasmonic field and optical sensor response at the location of maximal interaction with the gas molecules. While it cannot be excluded that a nonfractal TiO<sub>2</sub> morphology having a similar (very high) porosity of 98% may provide a similar enhancement, such a structure may be hardly fabricated without using fractals. Furthermore, while other morphologies, such as aerogels, may provide similarly high average porosities, the fractal structure has the further advantage of providing a hierarchical pore size distribution, which facilitates the penetration of the VOC molecules in the film and provides a large surface area for molecules' adsorption.

A key issue affecting the development of sensors, and in particular LSPR, for gas molecules measurement is the lack of selectivity against other gas molecules. The ability of a device to not only detect but also discern among different species is a highly desirable feature. Here, we take advantage of the molecular adsorption on the large and accessible fractal surface to identify the interacting VOC and achieve its selective sensing. At room temperature and standard humidity levels, there is a nonnegligible amount of gas molecules from the surrounding environment that condensates on the nanostructured surface. In addition, photoadsorbed reactive species (e.g., O<sub>2</sub><sup>-</sup>, O<sup>2-</sup>) on the TiO<sub>2</sub> surface (Figure S11, Supporting Information), which are formed under UV–vis illumination, can participate to the weak interactions and adsorption process of the VOCs on the TiO<sub>2</sub> surface. In particular, the interaction of EtOH with the TiO<sub>2</sub> surface has been widely investigated for catalysis. Different mechanisms have been proposed, and at room or low temperatures (<200 °C) the main pathway implicates the adsorption of EtOH through a hydroxyl group<sup>[31,32]</sup>. The adsorption initially takes place thanks to the O–H bond cleavage and is surface-structure independent.<sup>[31]</sup> This leads to the formation of CH<sub>3</sub>CH<sub>2</sub>O and H species that promptly react with the active oxygen on the TiO<sub>2</sub> surface. For acetone, the interaction with the TiO<sub>2</sub> surface is likely to involve the carbonyl group (C = O). Under UV–vis light, this interaction can be triggered by several photoadsorbed oxygen reactive species (O<sup>-</sup>), or simply with

the TiO<sub>2</sub> lattice oxygen.<sup>[33]</sup> For toluene, an aromatic hydrocarbon, the adsorption on the TiO<sub>2</sub> surface is configuration dependent,<sup>[34]</sup> i.e., the orientation of the benzoic ring can affect the interaction with the TiO<sub>2</sub>. If the toluene molecule has the benzoic ring planar to the surface, it will likely bind through the hydroxyl groups.<sup>[35]</sup> If the ring is orthogonal to the TiO<sub>2</sub> surface, the methyl group can dissociate and interact either with the lattice oxygen or photoadsorbed oxygen species. Such condensation increases the local refractive index near the surface of dielectric structures effectively increasing the LSPR response and device sensitivity. As the partial pressure of different gases is strongly dependent on the ambient temperature, this also provides a useful tool to discern among different VOCs by obtaining hyperspectral transmittance maps of our hybrid metasurface at different temperatures.

To test this concept, we exposed the optimal fractal-enhanced LSPR structures to three different exemplary VOCs, namely, ethanol, acetone, and toluene with increasing temperatures from 25 to 80 °C. **Figure 5a,b** shows the characteristic measured LSPR redshift at room temperature for 4 vol% acetone and toluene, respectively. Interestingly, we achieved a fast response of fractal-enhanced LSPR structures, in the order of 10 s, to all the tested VOCs. **Figure 5c** shows the high repeatability and sensitivity of the optical response with cyclic injection of toluene from 4 to 1 vol% at room temperature (**Figure 5c**).

An analysis of the optical response as a function of temperature and concentration is shown in **Figure 5d,e** for acetone and toluene, respectively. They describe the response of the optimized fractal-enhanced LSPR sensor as a function of both the temperature and the analytes concentration.

For any specific analyte, the higher the concentration the higher is its vapor pressure. Considering the adsorbed gas molecules on the ultraporous fractal and their kinetic energy distribution, at any given temperature, there is a nonzero probability that the intermolecular attractive forces between the fractal adsorbent and the gas are greater than those between molecules of the gas itself, resulting in a condensation. This in turn causes a substantial increase in the local refractive index  $n$ . In the case of toluene the condensed equilibrium thickness can be estimated from its vapor pressure within the Hamaker theory<sup>[36]</sup> and is evaluated to be 0.41 nm (see Section S12, Supporting Information). This corresponds to a total effective refractive index of 1.0116 calculated with the Bruggeman effective medium equation, which is an enhancement of more than two orders of magnitude in the decimal digits as compared to the refractive index of the air ( $n_{\text{air}} = 1.000292$ ). With no gas condensation, assuming the same VOC concentration, the calculated refractive index of the toluene–air gas mixture is 1.000315.

**Figure 5** shows the use of this condensation mechanism for selective sensing and identification of the injected VOC. The thin liquid layer present on all the surface of the system is responsible for the dramatic increase in the refractive index. Increasing the temperature increases the evaporation rate and decreases the condensation rate. This process leads to the reduction of the amount of VOC condensed, decreasing the change in refractive index, and resulting in a drop in the LSPR shift (**Figure 5d–g**). Notably, **Figure 5d,e** shows a further proof of the impact of the condensation mechanism on the sensing performance. Above the corresponding evaporation temperatures for

acetone and toluene of 56 °C and 111 °C (at standard condition), respectively, there is a negligible LSPR shift.

**Figure 5f** shows the LSPR shift as a function of the temperature for toluene. At any specific temperature the  $\Delta\lambda_{\text{LSPR}}$  decreases with decreasing toluene concentration. For any given VOCs the vapor pressure, which is directly correlated to the condensation rate, is a function of the temperature as stated from the Clausius–Clapeyron equation,<sup>[37]</sup> thus the amount of condensation is an intrinsic property of every different VOC. By using this hallmark, our sensors can differentiate with high selectivity analytes at very low concentrations. A normalization of the sensor response ( $\Delta\lambda_{\text{LSPR}}$ ) to its maximum value, at different concentrations and temperatures, shows the temperature induced decay of the optical responses for these three different VOCs. Notably, plotting the normalized LSPR shifts against the temperature leads to an overall exponential decay trend with decay rates depending on the analyte (**Figure 5g**). Fitting these experimental data with a vapor pressure-exponential decay model shows good correlation. It is observed that well-defined different decay rates for each VOC gas, respectively  $\tau_{\text{ethanol}} = 26 \pm 3$  °C,  $\tau_{\text{acetone}} = 7.4 \pm 0.3$  °C, and  $\tau_{\text{toluene}} = 12 \pm 3$  °C, are found. This allows to identify several analytes that induce similar variations in the local refractive index by analyzing the shape of the optical response decay induced by increasing the temperature. This opens the way for a new class of wireless optical gas sensors, working at low operating temperatures and providing high sensitivity and selectivity.

We have developed a novel nanostructured material, comprising resonant metasurfaces and tailored dielectric fractals, for enhancing the interaction of the plasmonic field with a gaseous environment. We demonstrate the use of this material for optical sensing of volatile molecules at room temperature, with superior sensitivity and selectivity. Notably, optimal dielectric–plasmonic structures are able to detect refractive index changes lower than  $8 \times 10^{-6}$  in a gas mixture, improving the lower limit of detection of the resonant metasurfaces by more than 30 times, achieving selective detection of gas molecules better than 0.1 vol%. This is attributed to the strong enhancement of the plasmonic near- and far-field in the porous dielectric fractal structures for thickness exceeding 1.8  $\mu\text{m}$ . Simultaneously, the large surface area of these fractals provide multiple means of controlling the interaction with gaseous molecules allowing not only the detection but also the identification of volatile organic compounds. We believe that the unique properties of these dielectric–plasmonic materials set the basis for the engineering of many novel optoelectronic and optochemical devices with application extending from photocatalysis to contactless non-invasive medical sensing.

## Experimental Section

Gold plasmonic metasurfaces were obtained through an HCL technique (see **Figure S1** in the Supporting Information for a schematic of the fabrication method).<sup>[38]</sup> Briefly, the fused silica substrates were cleaned in acetone and isopropyl alcohol and sonicated. PMMA was spun on the sample at 3000 rpm and soft baked in an oven furnace at 180 °C for 10 min. A quick oxygen plasma (50 W for 5 s) rendered the surface hydrophilic and a poly(diallyldimethylammonium chloride) (PDPA)–water solution (0.2%) was dispersed on the samples for 30 s and rinsed

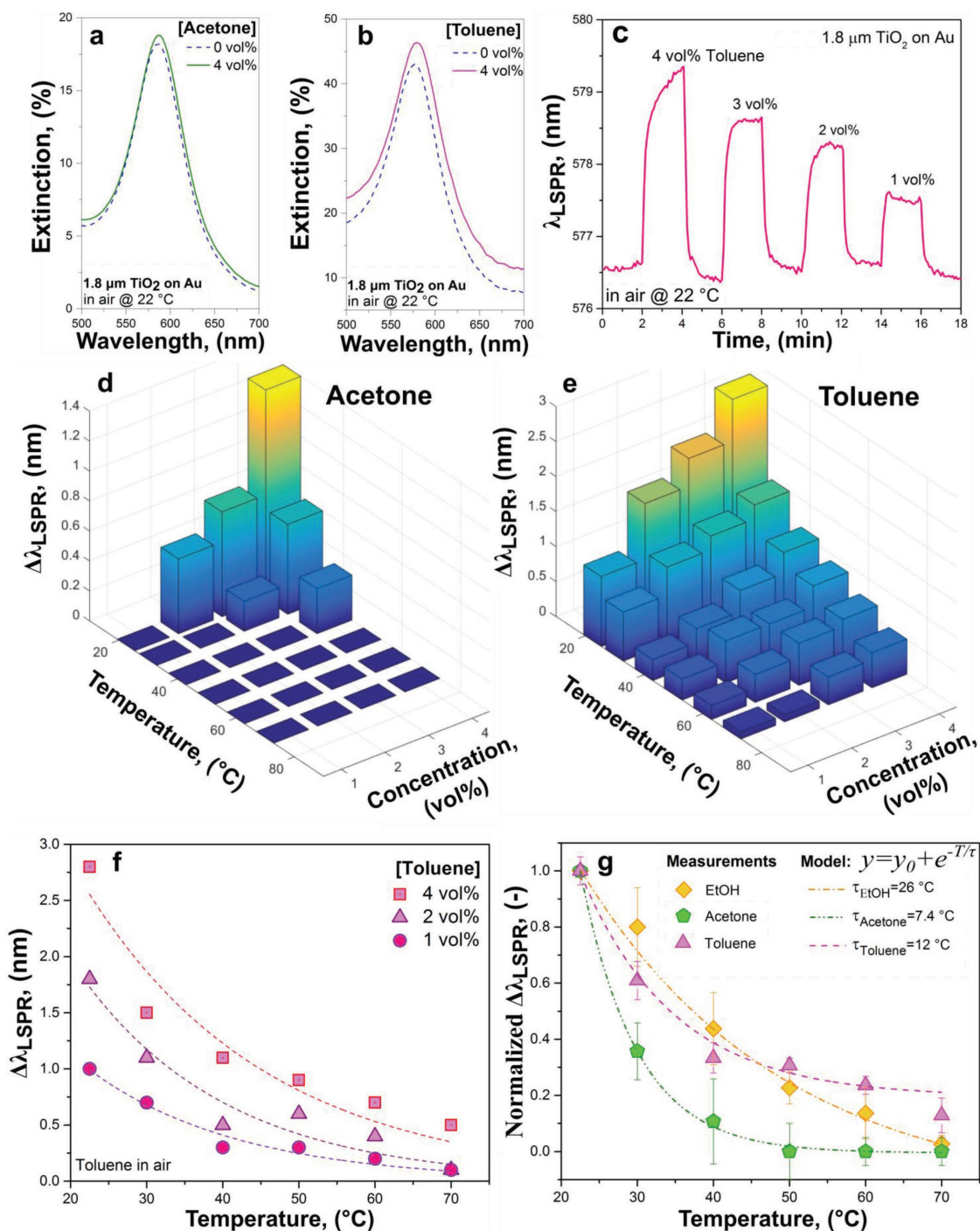


**Figure 5.** Condensation and selectivity. Extinction measurement in 0% and 4% a) acetone–air and b) toluene–air mixtures, mixtures for the hybrid 100 nm Au disks array functionalized with 1.8  $\mu\text{m}$  of  $\text{TiO}_2$ . (c) Dynamic responses of the same sample to different cycles of air/toluene at room temperature and at different concentrations show high repeatability and sensitivity. (d,e) Proof of the condensation mechanism for the LSPR sensing using the 1.8  $\mu\text{m}$  of  $\text{TiO}_2$  functionalization onto the 100 nm disks array: different VOCs were tested at different concentrations and temperatures. For any given concentration, the higher the temperature the smaller is the measured redshift due to evaporation of a condensed layer. (f) LSPR shift as a function of the temperature for different concentrations of toluene. The amount of the LSPR shift at each temperature is proportional to the gas concentration. (g) The condensation rate is unique to each gas and it depends on the vapor pressure. By normalizing the shifts and fitting the data as a function of the temperature we obtain different exponential decays with proper and well defined decay rates: this enables to discriminate between gases opening the road toward selectivity.

in deionized water for 10 s to positively charge the surface. Polystyrene beads with different diameters and diluted in water (0.1%) were subsequently dispersed for 3 min on the substrate by drop-casting and

successively rinsed for 30 s in running water. A 10 nm Au mask was deposited on the sample and the latex beads removed by tape stripping. The resulting Au mask was then used as a deposition mask. The PMMA

was first etched by O<sub>2</sub> plasma, at 50 W at 250 mTorr for 3 min. A 1 nm Ti adhesion layer and 40 nm Au were deposited. Lift-off in acetone at room temperature was performed. All samples were annealed air at 150 °C for 10 min prior to shipping. The different diameter sizes were determined by the initial polystyrene bead diameter utilized. Some test samples were imaged using a Zeiss Supra SEM and e-spacer to avoid charging effects. The tilted view SEM image in Figure 1 was obtained for a substrate fabricated as described above, but using a Silicon chip as an initial substrate to avoid charging effects. Linear extinction measurements in Figure S2 (Supporting Information) were obtained using a fiber coupled halogen lamp (HL-2000, Ocean Optics) as an illumination source and the light was collected by a fiber coupled spectrometer (BRC711E, B&W Tek). All measurements were normalized using the transmission through a bare fused silica substrate as a reference.

A flame spray pyrolysis setup was used for the synthesis and direct deposition of the TiO<sub>2</sub> fractal clusters on the Au nanodisk array. Titanium (IV) isopropoxide (TTIP, Sigma-Aldrich, purity > 97%) was diluted in xylene (Sigma-Aldrich) in order to produce a metal concentration of 0.2 mol L<sup>-1</sup>. The precursor solution was supplied at a constant rate of 5 mL min<sup>-1</sup> through a syringe pump and dispersed into a fine spray with 7 L min<sup>-1</sup> oxygen at a constant pressure drop of 2 bars. In both cases spray was ignited by supporting premixed methane/oxygen flames (CH<sub>4</sub> = 1.2 L min<sup>-1</sup>, O<sub>2</sub> = 2 L min<sup>-1</sup>) and the height above burner was set to 20 cm.

Topographical and optical characterization techniques were used to depict all the samples. Morphological characteristics were investigated with an analytical SEM, using Zeiss Ultraplus (FESEM) at 3 kV and the results were analyzed using the software ImageJ and its plugin FlaLac for the fractal analysis. Raman spectra were collected using a Renishaw inVia reflex spectrometer system equipped with a 532 nm laser radiation and a grating of 2400 l nm<sup>-1</sup>. TEM imaging of the flame-made TiO<sub>2</sub> nanoparticles was performed by a high-resolution field emission microscope Jeol 2100F and the particle size distribution was evaluated by counting 218 monomers with the help of the software ImageJ.

Extinction measurements were taken in real time using a linear transmittance setup equipped with a gas delivery system with controlled temperature and flow rate. An optimal focus of the beam was reached with a series of collimating and objective lenses, as well as adjustable apertures, from ThorLab. The beam was then delivered to a UV–vis cooled modular spectrometer Ocean Optics QE Pro.

Electrodynamics based on finite-difference time-domain were performed with commercially available software (Lumerical FDTD). Perfectly matched layers were employed as boundary conditions to avoid the wave reflection at the boundary. A total-field scattered-field source with a polarization along the *x*-axis and a propagation vector along the *z*-direction was chosen to excite from the backside of the structure. A nonuniform meshing refinement was used to guarantee a precise result with a smallest mesh cell of 0.2 nm to increase the accuracy of the simulation. Drude models were applied to the fused silica and TiO<sub>2</sub>, instead the optical properties of gold were taken from the Johnson and Christy.<sup>[39]</sup> The Au and TiO<sub>2</sub> dimensions were chosen to mimic the experimental results of the best response sample. The near-field enhancements at the resonance were then monitored using a set of frequency domain probes.

## Supporting Information

Supporting Information is available from the Wiley Online Library or from the author.

## Acknowledgements

The authors acknowledge the financial support by the Australian Research Council. A.T. gratefully acknowledges the support of the Australian Research Council DP150101939, the Australian Research Council DE160100569, and the Westpac 2016 Research Fellowship.

M.R. sincerely appreciates funding from the Australian Research Council DE 170100250. All the authors acknowledge the use of the Australian National Fabrication Facility (ANFF), ACT Node, as well as the Centre of Advanced Microscopy (CAM) at ANU.

## Conflict of Interest

The authors declare no conflict of interest.

## Keywords

fractals, metasurfaces, plasmonic sensors, selectivity, VOCs

Received: February 8, 2018

Revised: April 1, 2018

Published online:

- [1] J. N. Anker, W. P. Hall, O. Lyandres, N. C. Shah, J. Zhao, R. P. Van Duyne, *Nat. Mater.* **2008**, *7*, 442.
- [2] a) A. J. Haes, S. Zou, G. C. Schatz, R. P. Van Duyne, *J. Phys. Chem. B* **2004**, *108*, 6961; b) A. J. Haes, S. Zou, G. C. Schatz, R. P. Van Duyne, *J. Phys. Chem. B* **2004**, *108*, 109; c) A. V. Whitney, J. W. Elam, S. Zou, A. V. Zinovev, P. C. Stair, G. C. Schatz, R. P. Van Duyne, *J. Phys. Chem. B* **2005**, *109*, 20522; d) L. Chen, Y. Zhou, M. Wu, M. Hong, *Opto-Electron. Adv.* **2018**, *1*, 170001.
- [3] L. Tian, E. Chen, N. Gandra, A. Abbas, S. Singamaneni, *Langmuir* **2012**, *28*, 17435.
- [4] a) A. E. Cetin, D. Etezadi, B. C. Galarreta, M. P. Busson, Y. Eksioğlu, H. Altug, *ACS Photonics* **2015**, *2*, 1167; b) B. Spackova, P. Wrobel, M. Bockova, J. Homola, *Proc. IEEE* **2016**, *104*, 2380; c) A. Tittl, H. Giessen, N. Liu, *Nanophotonics* **2014**, *3*; d) T. Shegai, C. Langhammer, *Adv. Mater.* **2011**, *23*, 4409; e) A. V. Kabashin, P. Evans, S. Pastkovsky, W. Hendren, G. A. Wurtz, R. Atkinson, R. Pollard, V. A. Podolskiy, A. V. Zayats, *Nat. Mater.* **2009**, *8*, 867; f) S. S. Aćimović, M. P. Kreuzer, M. U. González, R. Quidant, *ACS Nano* **2009**, *3*, 1231; g) J. C. Sharpe, J. S. Mitchell, L. Lin, N. Sedoglavich, R. J. Blaikie, *Anal. Chem.* **2008**, *80*, 2244.
- [5] A. Tricoli, N. Nasiri, S. De, *Adv. Funct. Mater.* **2017**, *27*, 1605271.
- [6] a) M. S. Yavuz, Y. Cheng, J. Chen, C. M. Copley, Q. Zhang, M. Rycenga, J. Xie, C. Kim, K. H. Song, A. G. Schwartz, *Nat. Mater.* **2009**, *8*, 935; b) L. Scarabelli, M. Coronado-Puchau, J. J. Giner-Casares, J. Langer, L. M. Liz-Marzán, *ACS Nano* **2014**, *8*, 5833; c) G. J. Nusz, S. M. Marinakos, A. C. Curry, A. Dahlin, F. Hook, A. A. Wax, A. Chilkoti, *Anal. Chem.* **2008**, *80*, 984; d) I. Ament, J. Prasad, A. Henkel, S. Schmachtel, C. Sönnichsen, *Nano Lett.* **2012**, *12*, 1092; e) H. H. Jeong, A. G. Mark, M. Alarcon-Correa, I. Kim, P. Oswald, T. C. Lee, P. Fischer, *Nat. Commun.* **2016**, *7*, 11331; f) N. Liu, M. Mesch, T. Weiss, M. Hentschel, H. Giessen, *Nano Lett.* **2010**, *10*, 2342; g) M. Hentschel, D. Dregely, R. Vogelgesang, H. Giessen, N. Liu, *ACS Nano* **2011**, *5*, 2042; h) R. Adato, A. A. Yanik, J. J. Arnsden, D. L. Kaplan, F. G. Omenetto, M. K. Hong, S. Erramilli, H. Altug, *Proc. Natl. Acad. Sci.* **2009**, *106*, 19227.
- [7] S. S. Aćimović, H. Šípová, G. Emilsson, A. B. Dahlin, T. J. Antosiewicz, M. Käll, *Light: Sci. Appl.* **2017**, *6*, e17042.
- [8] N. Liu, M. L. Tang, M. Hentschel, H. Giessen, A. P. Alivisatos, *Nat. Mater.* **2011**, *10*, 631.
- [9] J. M. Bingham, J. N. Anker, L. E. Kreno, R. P. V. Duyne, *J. Am. Chem. Soc.* **2010**, *132*, 17358.
- [10] D. Buso, M. Guglielmi, A. Martucci, G. Mattei, P. Mazzoldi, C. Sada, M. L. Post, *Nanotechnology* **2006**, *17*, 2429.

- [11] a) D. Buso, M. Post, C. Cantalini, P. Mulvaney, A. Martucci, *Adv. Funct. Mater.* **2008**, *18*, 3843; b) E. Della Gaspera, M. Guglielmi, S. Agnoli, G. Granozzi, M. L. Post, V. Bello, G. Mattei, A. Martucci, *Chem. Mater.* **2010**, *22*, 3407; c) E. Della Gaspera, A. Martucci, *Sensors* **2015**, *15*, 16910.
- [12] a) M. Ando, *TrAC, Trends Anal. Chem.* **2006**, *25*, 937; b) M. Ando, T. Kobayashi, S. Iijima, M. Haruta, *Sens. Actuators, B* **2003**, *96*, 589.
- [13] a) B. Mehta, K. D. Benkstein, S. Semancik, M. E. Zaghoul, *Sci. Rep.* **2016**, *6*, 21287; b) P. Wang, M. Xia, O. Liang, K. Sun, A. F. Cipriano, T. Schroeder, H. Liu, Y.-H. Xie, *Anal. Chem.* **2015**, *87*, 10255.
- [14] a) J. R. Krenn, *Nat. Mater.* **2003**, *2*, 210; b) X. Guo, M. Qiu, J. Bao, B. J. Wiley, Q. Yang, X. Zhang, Y. Ma, H. Yu, L. Tong, *Nano Lett.* **2009**, *9*, 4515.
- [15] M. Barth, S. Schietinger, S. Fischer, J. Becker, N. Nüsse, T. Aichele, B. Löchel, C. Sönnichsen, O. Benson, *Nano Lett.* **2010**, *10*, 891.
- [16] O. Sánchez-Sobrado, G. Lozano, M. E. Calvo, A. Sánchez-Iglesias, L. M. Liz-Marzán, H. Míguez, *Adv. Mater.* **2011**, *23*, 2108.
- [17] A. Tricoli, S. E. Pratsinis, *Nat. Nanotechnol.* **2010**, *5*, 54.
- [18] B. Fazio, P. Artoni, M. Antonia Iatì, C. D'Andrea, M. J. Lo Faro, S. Del Sorbo, S. Pirotta, P. Giuseppe Gucciardi, P. Musumeci, C. Salvatore Vasi, R. Saija, M. Galli, F. Priolo, A. Irrera, *Light: Sci. Appl.* **2016**, *5*, e16062.
- [19] S. M. J. L. Castillo, D. Rodriguez-Perez, A. Perea, P. L. Garcia-Ybarra, *KONA Powder Part. J.* **2014**, *31*, 214.
- [20] N. Nasiri, T. D. Elmoe, Y. Liu, Q. H. Qin, A. Tricoli, *Nanoscale* **2015**, *7*, 9859.
- [21] D. Rodríguez-Pérez, J. L. Castillo, J. C. Antoranz, *Phys. Rev. E* **2005**, *72*, 021403.
- [22] G. Beauceage, H. K. Kammler, R. Mueller, R. Strobel, N. Agashe, S. E. Pratsinis, T. Narayanan, *Nat. Mater.* **2004**, *3*, 370.
- [23] a) G. Wang, C. M. Sorensen, *Appl. Opt.* **2002**, *41*, 4645; b) C. M. Sorensen, *Aerosol Sci. Technol.* **2001**, *35*, 648; c) A. P. C. Castelnovo, P. Piseri, P. Milani, *Phys. Rev. E* **2002**, *65*, 055102(R).
- [24] a) E. Goudeli, M. L. Eggersdorfer, S. E. Pratsinis, *Langmuir* **2015**, *31*, 1320; b) L. de Martín, W. G. Bouwman, J. R. van Ommen, *Langmuir* **2014**, *30*, 12696.
- [25] J. H. Scheckman, P. H. McMurry, S. E. Pratsinis, *Langmuir* **2009**, *25*, 8248.
- [26] G. B. Jingyu Hyeon-Lee, S. E. Pratsinis, S. Vemury, *Langmuir* **1998**, *14*, 5751.
- [27] W. S. Y. Wong, G. Liu, N. Nasiri, C. Hao, Z. Wang, A. Tricoli, *ACS Nano* **2017**, *11*, 587.
- [28] A. Tricoli, M. Righettoni, S. E. Pratsinis, *Nanotechnology* **2009**, *20*, 315502.
- [29] K. V. Sreekanth, Y. Alapan, M. Elkabbash, E. Ilker, M. Hinczewski, U. A. Gurkan, A. De Luca, G. Strangi, *Nat. Mater.* **2016**, *15*, 621.
- [30] a) M. Lutz, A. L. Anshuman, K. F. Sheldon, *Nanotechnology* **2006**, *17*, 4783; b) J. A. H. Dreyer, N. Riefler, G. R. Pesch, M. Karamehmedovi, U. Fritsching, W. Y. Teoh, L. Mädler, *Chem. Eng. Sci.* **2014**, *105*, 69.
- [31] R. Zhang, Z. Liu, L. Ling, B. Wang, *Appl. Surf. Sci.* **2015**, *353*, 150.
- [32] a) P. M. Jayaweera, E. L. Quah, H. Idriss, *J. Phys. Chem. C* **2007**, *111*, 1764; b) M. C. Holz, K. Tolle, M. Muhler, *Catal. Sci. Technol.* **2014**, *4*, 3495.
- [33] a) M. El-Maazawi, A. N. Finken, A. B. Nair, V. H. Grassian, *J. Catal.* **2000**, *191*, 138; b) Y. Wang, C. Woll, *Chem. Soc. Rev.* **2017**, *46*, 1875.
- [34] F. Zhang, X. Zhu, J. Ding, Z. Qi, M. Wang, S. Sun, J. Bao, C. Gao, *Catal. Lett.* **2014**, *144*, 995.
- [35] S. Neubert, A. Ramakrishnan, J. Strunk, H. Shi, B. Mei, L. Wang, M. Bledowski, D. A. Guschin, M. Kauer, Y. Wang, M. Muhler, R. Beranek, *ChemPlusChem* **2014**, *79*, 163.
- [36] W. S. Y. Wong, T. Gengenbach, H. T. Nguyen, X. Gao, V. S. J. Craig, A. Tricoli, *Adv. Funct. Mater.* **2017**, *28*, 1704423.
- [37] M. S. Silberberg, *Principles of General Chemistry*, McGraw-Hill, New York **2007**.
- [38] H. Fredriksson, Y. Alaverdyan, A. Dmitriev, C. Langhammer, D. S. Sutherland, M. Zäch, B. Kasemo, *Adv. Mater.* **2007**, *19*, 4297.
- [39] P. B. Johnson, R.-W. Christy, *Phys. Rev. B* **1972**, *6*, 4370.